Review Article | Technology, Experiment, and Physics

eISSN 2005-8330
https://doi.org/10.3348/kjr.2020.0144
Korean J Radiol 2021;22(1):86-96

Korean Journal of Radiology
KJR

Spectral Computed Tomography: Fundamental Principles and Recent Developments

Aaron So, PhD[1, 2], Savvas Nicolaou, MD[3, 4]

[1]Imaging Program, Lawson Health Research Institute, London, Canada; [2]Department of Medical Biophysics, University of Western Ontario, London, Canada; [3]Department of Emergency and Trauma Imaging, Vancouver General Hospital, Vancouver, Canada; [4]Department of Radiology, University of British Columbia, Vancouver, Canada

CT is a diagnostic tool with many clinical applications. The CT voxel intensity is related to the magnitude of X-ray attenuation, which is not unique to a given material. Substances with different chemical compositions can be represented by similar voxel intensities, making the classification of different tissue types challenging. Compared to the conventional single-energy CT, spectral CT is an emerging technology offering superior material differentiation, which is achieved using the energy dependence of X-ray attenuation in any material. A specific form of spectral CT is dual-energy imaging, in which an additional X-ray attenuation measurement is obtained at a second X-ray energy. Dual-energy CT has been implemented in clinical settings with great success. This paper reviews the theoretical basis and practical implementation of spectral/dual-energy CT.

Keywords: *X-rays; Computed tomography; Spectral; Dual energy*

INTRODUCTION

X-ray computed tomography (CT) has continued to evolve since its introduction as a noninvasive diagnostic tool half a century ago. One of the main subject areas of ongoing research in the field of CT is spectral imaging, which refers to the use of energy information in polychromatic X-rays for optimizing tissue characterization. While spectral CT had its roots in the dawn of the CT era, its application in real-world clinical settings has increasingly emerged over the last decade as key technological advances have increased its clinical feasibility. Dual-energy CT is a subset of spectral CT that specifically refers to the use of two X-ray energy spectra for imaging. It is the most common form of spectral CT used in clinical applications, and it represents a compromise between true energy-resolving imaging and current technological limitations. Nevertheless, the successful application of dual-energy CT has provided us with a glimpse into the full capability of spectral CT in the future. In this paper, we will review the fundamental principles, recent developments, and current and emerging clinical applications of dual-energy/spectral CT.

Received: February 19, 2020 **Revised:** April 10, 2020
Accepted: April 13, 2020
Corresponding author: Aaron So, PhD, Imaging Program, Lawson Health Research Institute, 268 Grosvenor Street, London N6A 4V2, Canada.
• E-mail: aso@robarts.ca

Scanner Configuation and Acquisition Mode

All clinical CT scanners that are currently capable of dual-energy acquisition can be classified into two main categories: source-based and detector-based. Source-based scanners use X-ray beams with different energy spectra for imaging. This function can be achieved by employing either two independent X-ray tubes with each tube operating at a different tube potential or a single X-ray tube capable of rapidly switching between low and high tube potentials. The detector-based scanners rely on the energy-resolving power of the X-ray detector to separate the signals that correspond with low-energy X-ray photons from those associated with high-energy photons. This separation can be achieved by using a photon-counting detector or a dual-layer energy-integrating detector with a different X-ray

Korean Journal of Radiology
KJR

stopping power in each layer. The designs and acquisition methods of each type of scanner are briefly discussed in the following sections.

Dual-Source Scanner

One source-based approach for dual-energy imaging is through implementation of a dual-source system (e.g., SOMATOM Force, Siemens Healthineers) (Fig. 1A), in which two independent source-detector pairs are mounted to the same gantry at about a 90° offset (1, 2). While one X-ray tube operates at a low tube potential, the other tube operates at a high tube potential (e.g., 70 kV vs. 120 kV). This scanner design has several notable advantages for dual-energy imaging. First, the tube current can be optimized individually to ensure a comparable noise level between the low- and high-energy projection sets. Second, an additional filter (e.g., a tin filter) can be used in one tube to further enhance the separation between the two energy spectra. A limitation of this scanner configuration is that one detector is restricted to a smaller scan field of view than the other (33 cm vs. 50 cm) (3). Another issue is that significant photon cross-scattering occurs when two X-ray tubes operate simultaneously, although advanced algorithms have been developed to correct for the increased projection noise arising from photon cross-scattering (4, 5). Furthermore, due to significant mismatch of view angles between the low- and high-energy projection sets, information related to material decomposition may be affected, especially if patient movement (e.g., cardiac and/or respiratory motion) occurs during the two acquisitions.

Single-Source Scanner Capable of Ultrafast Potential Switching

A different source-based approach is through the

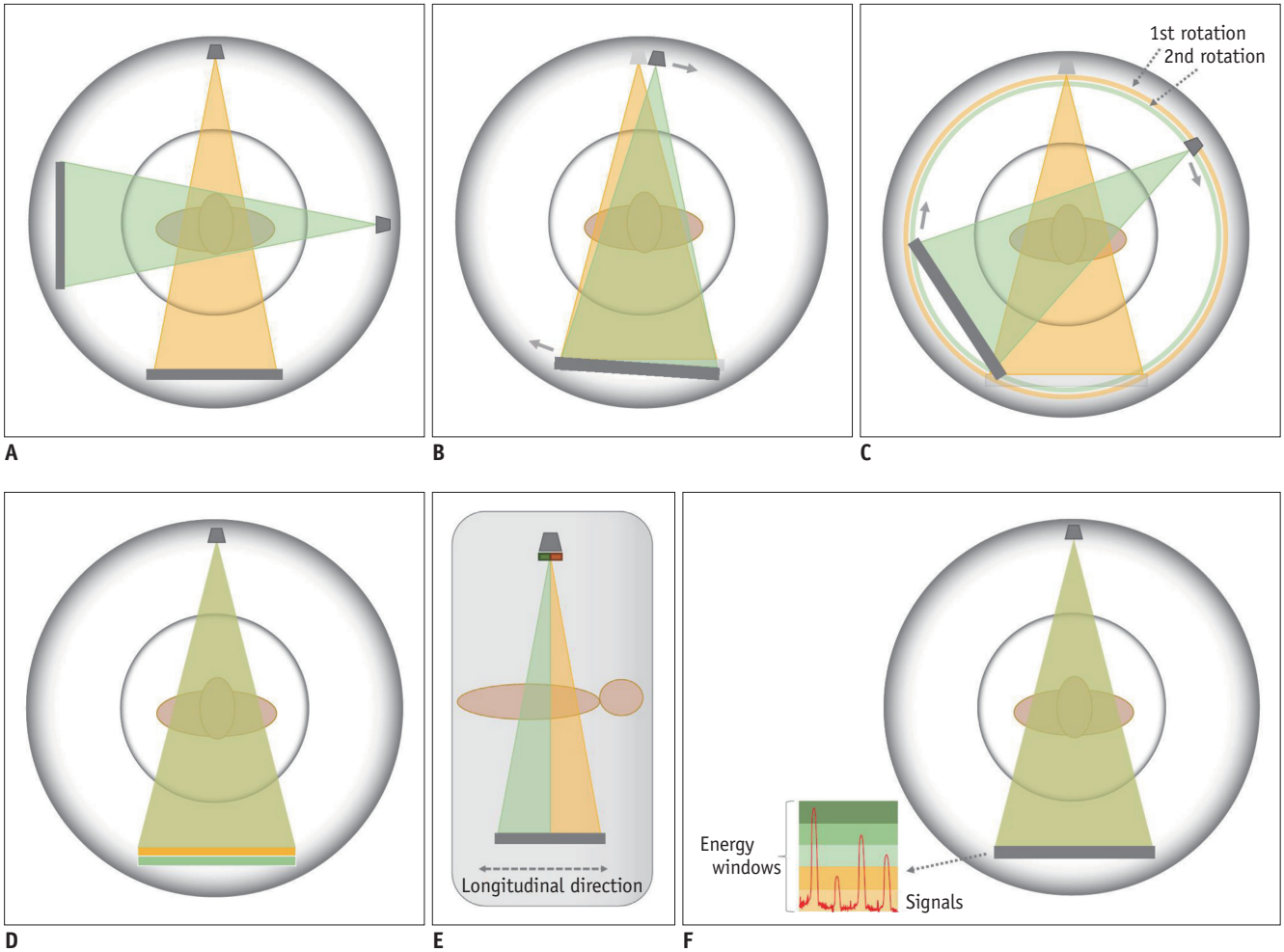

Fig. 1. CT scanner systems that are currently available for dual-energy/spectral imaging.
A. Dual-source. **B.** Single-source with ultrafast kV switching. **C.** Single-source without ultrafast kV switching. **D.** Single-source with dual-layer detector. **E.** Single-source with split-filter. **F.** Single-source with photon-counting detector. CT = computed tomography

https://doi.org/10.3348/kjr.2020.0144

implementation of a single X-ray tube capable of repetitively switching between low and high tube potentials within a full gantry rotation period (e.g., Discovery CT750 HD, GE Healthcare) (Fig. 1B) (6, 7). Since the switching of tube potential occurs extremely fast (approximately every 0.2 milliseconds), the 80-kV and 140-kV projection sets are practically acquired from the same view angle. The minimal mismatch of view angles between low- and high-energy projection sets due to the near-simultaneous acquisition facilitates performance of material decomposition in the projection domain, which theoretically results in a more exact beam-hardening correction in the measured projections and material decomposition, as shown in previous studies (8). However, a limitation of this system is the relatively high overlap of the energy spectra. To reduce spectral contamination between rapid consecutive acquisitions, a scintillating material that has an ultrafast primary decay time and a very low afterglow (delayed fluorescence) is used for the X-ray detector elements (9, 10). Another limitation associated with this system is that the tube current cannot be modulated as fast as the tube potential; therefore, the tube current cannot be independently adjusted for each tube potential. An equivalent method to optimize the tube current for each tube potential is to modulate the duration of exposure (X-ray fluence) at each tube potential in order to achieve optimal image quality without dose penalty (6, 11).

Single-Source Scanner without Ultrafast Potential Switching

An alternative approach for dual-energy imaging by a single-source scanner is through switching the tube potential between successive gantry rotations in an axial or helical (spiral) mode rather than within each gantry rotation (e.g., Aquilion One, Canon Medical Systems) (Fig. 1C) (12, 13). While the projection sets corresponding to different energy levels can be acquired at exactly the same view angle, this acquisition method is considered to be less ideal than the rapid kV-switching method, especially for cardiac and abdominal applications, since cardiac and respiratory motion during the two full gantry rotations may induce larger degrees of inconsistency in the two energy projection sets.

Single-Source Scanner with Dual-Layer Detector

Compared to the three systems discussed above, a system equipped with a single X-ray tube and a layered X-ray detector bears perhaps the closest resemblance to the ideal energy-resolving photon-counting system because the low- and high-energy X-ray photons from a single polychromatic X-ray beam can be separated simultaneously (e.g., IQon Spectral CT, Philips Healthcare) (Fig. 1D) (14, 15). The layered detector is made of two materials with different X-ray attenuation properties. In this configuration, the material with the lower stopping power (yttrium-based garnet) is placed above the material with the higher stopping power (gadolinium oxysulphide) (16). This design allows low-energy X-ray photons to be predominately collected from the top detector layer and high-energy photons to be collected from the bottom detector layer. The main advantage of this approach is that the low- and high-energy projection sets are acquired simultaneously at identical view angles, which facilitates a more accurate material decomposition. Furthermore, the inconsistent noise level associated with the low- and high-energy projection sets can be corrected by changing the thicknesses of the two detector layers (17). However, the mechanism of this dual-energy acquisition technique relies on the assumptions that all the low-energy photons are attenuated in the top detector layer and that the high-energy photons do not interact with the top layer material during transit to the bottom detector layer. Violation of these assumptions results in a suboptimal spectral separation between the low- and high-energy data and an inaccurate material decomposition (14).

Single-Source Scanner with Split-Filter

More recently, a vendor has introduced a new technique of acquiring dual-energy projections from a single-source scanner by placing a split filter directly in front of the X-ray tube (e.g., TwinBeam Dual-Energy technology in SOMATOM Edge, Siemens Healthineers) (Fig. 1E) (18). The split filter is composed of gold and tin stacked adjacent to each other in the longitudinal direction in order to achieve spectral separation of a polychromatic beam of X-rays. For instance, at the 120-kV energy spectrum, filtration with gold and tin leads to a low-energy spectrum with a mean photon energy of 68 keV and a high-energy spectrum with a mean energy of 86 keV, respectively. The main advantage of this technology is that many current clinical CT scanners can easily be upgraded with an add-on split filter to perform dual-energy imaging. However, the spectral separation achieved with the split filter is relatively subtle compared to the separation achieved with a dual-source scanner, leading

https://doi.org/10.3348/kjr.2020.0144

Korean Journal of Radiology
KJR

to inferior performance of material decomposition (19).

Single-Source Scanner with Energy-Resolving Detector

All the aforementioned CT systems use "energy-integrating" X-ray detectors and therefore require an additional beam, detector, and/or filter to achieve spectral separation of the X-ray photons. A photon-counting CT system takes a completely different approach by using a detector capable of resolving the energies of individual photons directly from a polychromatic X-ray beam (Fig. 1F) (20-22). The materials used for making energy-resolving detectors are different from those of energy-integrating detectors, and these differences are discussed in more detail in the next section. One advantage of this energy-resolving capability is that the detected X-ray photons can be categorized into a number of preset energy threshold levels to achieve multi-energy imaging (in contrast to the current techniques that are limited to dual-energy imaging). Furthermore, the energy thresholds can be set at levels that are above the system's electronic noise level to eliminate the noise in measured projections. Hence, photon-counting CT is more dose efficient compared to the current dual-energy CT techniques and is the subject of active ongoing research. Currently, there are at least two main CT vendors (Siemens Healthineers and Philips Healthcare) that have developed prototype photon-counting CT systems, and the initial results acquired with these systems are encouraging (23, 24).

X-Ray Detectors

Radiation detectors have a crucial role in dual-energy/spectral CT; therefore, a brief overview of the types of radiation detectors is provided here. In general, there are three types of detector that can detect ionizing radiation. The simplest form is a gas-filled detector, which consists of a chamber filled with an inert gas between two electrodes (such as a Geiger-Müller tube) (25). When a beam of X-rays strikes the chamber, the gas within it is ionized, and the resulting charged particles are collected by the electrodes, leading to electrical signals that can be recorded and digitized. Gas-filled detectors are primarily used for measurements of radiation dose (26). For diagnostic imaging, the radiation detector elements are composed of either solid-state scintillators or semiconductors. Scintillators are generally used for clinical CT scanners, while semiconductors are used in prototype photon-counting CT scanners that are not yet clinically available.

Scintillators are materials that emit visible or ultraviolet light after interacting with ionizing radiation. When an incident X-ray photon strikes a crystalline scintillator, the photoelectric effect occurs, and the resulting photoelectron travels a short distance within the scintillator during which time its energy is deposited to the surrounding electrons. The excited electrons eventually return to their respective ground energy levels and emit characteristic radiation in the form of visible or ultraviolet light. These secondary light photons are collected by a photodiode, which then generates an electrical signal with a magnitude proportional to the total energy deposited by the light photons within a measurement interval (Fig. 2A).

One technical issue associated with the rapid kV-switching technique is spectral contamination (cross-talk) between the two energy data sets. To overcome this problem, one vendor has introduced a new scintillating material (garnet crystalline and rare earth phosphor composition) for the X-ray detector element, which is the first of its kind in the past two decades. This synthesized material has superior optical properties, including a faster primary speed and a shorter afterglow, than the cadmium tungstate and gadolinium oxysulfide (Gd_2O_2S) that are commonly used for

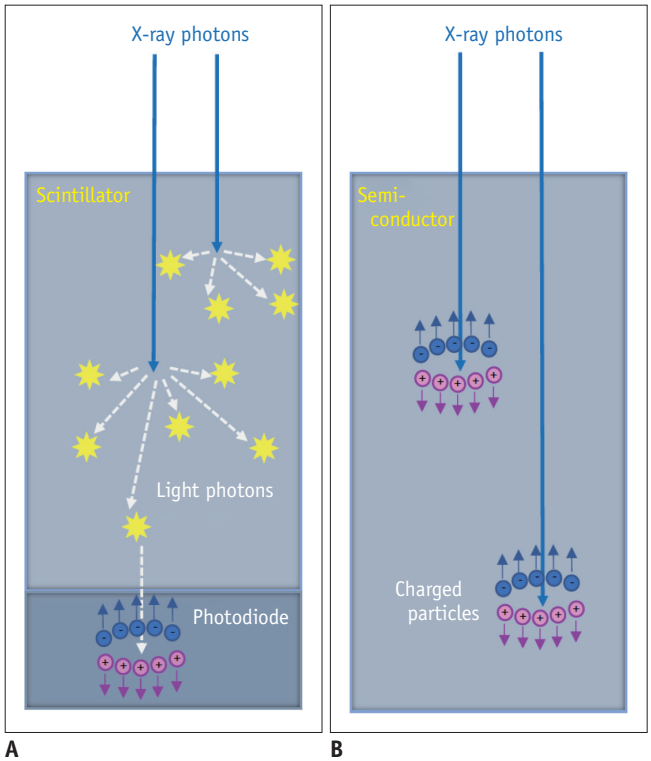

Fig. 2. (A) Scintillator-based energy-integrating detector versus (B) semiconductor-based photon counting detector.

https://doi.org/10.3348/kjr.2020.0144

solid-state detectors currently (27, 28). Primary speed refers to the time required for an excited electron to return to its ground energy state, which is dependent on the atom's electron configuration (9). Commonly, a small fraction of excited electrons will remain at a high-energy state for a longer period of time before returning to the ground energy state due to impurities in the scintillating crystal. Afterglow is the measure of this prolonged decay time (10). Hence, both primary speed and afterglow determine a detector's ability to differentiate successive signals from rapid acquisitions. This new detector material has an ultrafast primary speed (0.03 microseconds, which is 100 times faster than the commonly used Gd_2O_2S) and a low degree of afterglow (25% lower than Gd_2O_2S), which is crucial for minimizing the overlap between low- and high-energy projections acquired in successive views that are less than 0.5 milliseconds apart (29).

Semiconductors are materials with electrical conductivities lower than metals but higher than insulators. According to quantum physics, the electrons of an atom have discrete energy levels (bands). In a semiconducting material, the electrons that occupy the outermost energy band (valence band) can be raised to the next highest energy band (conduction band) if they are given external energy (such as from incident X-rays) to overcome the forbidden energy gap between the two bands. The conduction-band electrons are mobile and have high electrical conductivity. When an electron leaves the valence band to reside in the conduction band, it leaves behind a hole in the valence band with a net positive charge; hence, a pair of positive and negative charges (hole-electron) is produced (30). Due to the external voltage applied to the semiconductor, the negatively and positively charged particles generated from an X-ray interaction are rapidly pulled in the opposite direction and registered as an electrical signal by the electronic readout circuit (Fig. 2B). It is noteworthy that a semiconductor is usually doped with a small amount of impurities to reduce the magnitude of current induced by the applied external voltage in order to facilitate detection of weaker radiation-induced signals.

The electrical signal generated from each X-ray interaction in a semiconductor-based detector can be recorded individually, and the magnitude of this signal is directly proportional to the energy deposited by the incident X-ray photon. To achieve multi-energy imaging, the electronic system can apply multiple energy thresholds and can count the number of electrical pulses that fall into each energy bin in order to categorize the X-ray photons according to their energy levels (30). Additionally, the lowest energy threshold can be set at a level above the electronic noise level to eliminate the electronic noise in the signal counts. This is a notable advantage of photon-counting detectors in contrast to energy-integrating detectors, in which all photon energies and electronic noise within the measurement interval are combined.

One of the biggest challenges for photon-counting CT is the pulse pile-up effect, which refers to a phenomenon whereby two consecutive X-ray photons impinging on a detector within a short time interval are registered either as a single signal with a magnitude proportional to the sum of the energies of the two incident X-ray photons or as two partially overlapping signals, with corresponding signal-magnitude distortions (31). The pulse pile-up effect arises from the extremely high count rates encountered in CT (on the order of 10^9 per second per square millimeter) (32). If not corrected properly, this effect can lead to significant count loss and degradation in energy resolution. Another significant challenge for photon-counting CT is the cross-talk effect, which refers to spectral contamination from neighboring detector elements (33, 34). This effect manifests in a scenario where X-ray interaction occurs near the border of the two detector elements, and the resulting cloud of charge particles "spills" from one detector element to the adjacent detector element. Scattered X-ray photons can also contribute to the cross-talk effect, since the photons deflected from the original path may carry a fraction of the incident energy and deposit again in a different location. Cross-talk may lead to signal double counting and a loss of spatial resolution.

To date, the most promising materials for photon-counting detectors in CT appear to be cadmium zinc telluride (CZT), cadmium telluride (CdTe), and silicon (14, 23, 24, 35). Compared to silicon, CZT and CdTe have superior photon-absorption efficiencies due to their higher effective atomic numbers, which also reduces Compton scattering and signal double counting. However, the inferior charge-carrier mobilities of CZT and CdTe relative to silicon leads to a more severe pile-up at high count rates. The costs of CZT and CdTe production are also higher compared to silicon. Different calibration methods and correction factors have been proposed to tackle the errors in photon-counting CT that arise from the pulse pile-up and cross-talk effects, and these technical challenges must be overcome for the clinical implementation of photon-counting CT.

https://doi.org/10.3348/kjr.2020.0144

Korean Journal of Radiology
KJR

Image-Processing Algorithms

In this section, we review the theoretical basis for the reconstruction of material-density images (such as iodine-equivalent and water-equivalent images) and virtual monochromatic images from a set of low- and high-energy projections acquired with the CT systems discussed above.

Material-Density Images

Within the energy range of X-ray photons encountered in diagnostic CT examinations, the X-ray interaction in any material can be approximately represented by a linear combination of the photoelectric effect and the incoherent Compton scattering, barring the K-edge effect (36):

$$\left(\frac{\mu}{\rho}\right)(E) = \alpha_p f_\rho(E) + \alpha_c f_c(E) \quad [1]$$

where μ is the linear attenuation coefficient of the material at photon energy E; ρ is the density of the material that is energy independent; α_p and α_c are the coefficients that describe the relative contributions from the photoelectric effect and Compton scattering, respectively; and f_p and f_c are the functions that describe the photoelectric effect and Compton scattering, respectively. Both f_p and f_c are energy dependent and have been previously determined using experimental data. Specifically, f_p was found to be inversely proportional to the cubic of photon energy, and f_c was found to be a complex function (also called the Klein-Nishina function) (36). Alternatively, X-ray interaction in any material can be represented by two basis materials that are sufficiently different in their atomic numbers so as to have different X-ray interaction properties. A common choice for the basis-material pair is iodine-water, and Equation [1] can be rewritten as follows (37):

$$\left(\frac{\mu}{\rho}\right)(E) = \sigma_I \left(\frac{\mu}{\rho}\right)_I(E) + \sigma_W \left(\frac{\mu}{\rho}\right)_W(E) \quad [2]$$

where $\left(\frac{\mu}{\rho}\right)_I$ and $\left(\frac{\mu}{\rho}\right)_W$ are the mass attenuation coefficients of iodine and water, respectively, and σ_I and σ_W are the coefficients related to the contributions of X-ray interaction from iodine and water, respectively. Equation [2] can be further rewritten in the following form:

$$\mu(E) = \sigma_I \rho \left(\frac{\mu}{\rho}\right)_I(E) + \sigma_W \rho \left(\frac{\mu}{\rho}\right)_W(E) \quad [3]$$

Here, $\sigma_I\rho$ and $\sigma_W\rho$ are the equivalent densities (in gram per cm^3) of the basis materials, iodine and water, respectively (Fig. 3). The line integral over the linear attenuation coefficient in the X-ray path $\vec{r}$ can be expressed as:

$$\int \mu(\vec{r}, E)ds = \int \sigma_I \rho(\vec{r})ds \cdot \left(\frac{\mu}{\rho}\right)_I(E) + \int \sigma_W \rho(\vec{r})ds \cdot \left(\frac{\mu}{\rho}\right)_W(E)$$
$$= D_I \cdot \left(\frac{\mu}{\rho}\right)_I(E) + D_W \cdot \left(\frac{\mu}{\rho}\right)_W(E) \quad [4]$$

Here, D_I and D_W denote the line integral of the equivalent densities of iodine and water, respectively, and both parameters have a unit of gram per cm^2. In dual-energy imaging, projection measurements at each view angle are acquired with two different energy spectra yielding two nonlinear equations along each X-ray path:

$$P_L = -ln\left(\frac{I}{I_o}\right)_L = -\ln\left\{\int \Omega_L(E) e^{-\left[D_I \cdot \left(\frac{\mu}{\rho}\right)_I(E_L) + D_W \cdot \left(\frac{\mu}{\rho}\right)_W(E_L)\right]} dE \Big/ \int \Omega(E_L)dE\right\}$$

and

$$P_H = -ln\left(\frac{I}{I_o}\right)_H = -\ln\left\{\int \Omega(E_H) e^{-\left[D_I \cdot \left(\frac{\mu}{\rho}\right)_I(E_H) + D_W \cdot \left(\frac{\mu}{\rho}\right)_W(E_H)\right]} dE \Big/ \int \Omega(E_H)dE\right\} \quad [5]$$

in which the subscripts L and H represent the low- and high-energy spectra, respectively; P_L and P_H represent the measured projections at the low- and high-energy spectra, respectively; I and Io are the transmitted and incident X-ray

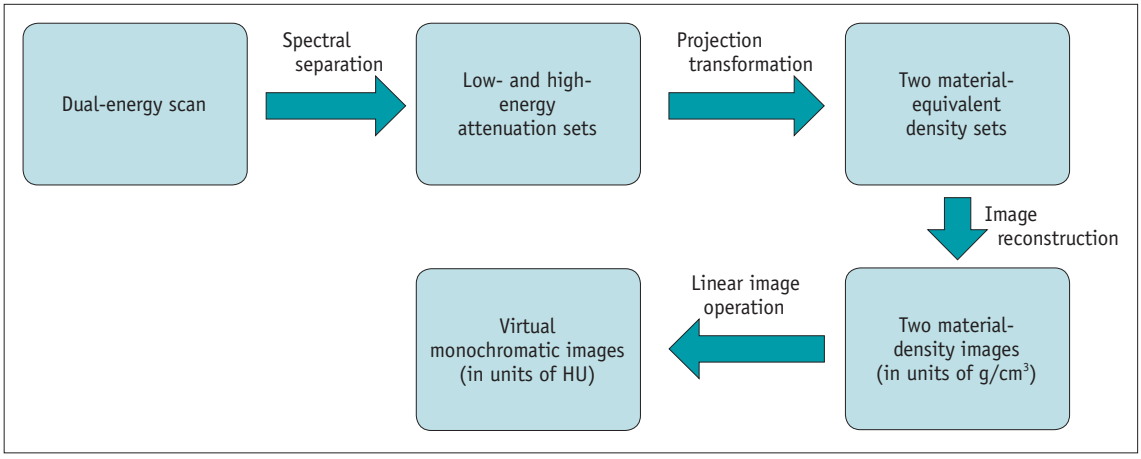

Fig. 3. Flow diagram for generation of material-density and virtual monochromatic images from a dual-energy scan.

https://doi.org/10.3348/kjr.2020.0144

intensities (or fluence), respectively; and $\Omega(E_L)$ and $\Omega(E_H)$ are the incident X-ray energy spectra that correspond to the low and high tube potentials, respectively. The mass attenuation coefficients of iodine and water correspond to any X-ray energy within the diagnostic range and are readily available in published tables (38). Hence, the only unknown quantities in Equation [5] are the equivalent densities of iodine and water, which can be approximately estimated using polynomial expansions (39):

$$\sigma_I\rho(\vec{r}) \approx c_1P_H + c_2P_L + c_3P_HP_L + c_4P_H^2 + c_5P_L^2 + \cdots$$

and

$$\sigma_W\rho(\vec{r}) \approx c_1P_H + c_2P_L + c_3P_HP_L + c_4P_H^2 + c_5P_L^2 + \cdots \quad [6]$$

where c_1 to c_5 are the polynomial coefficients. The nonlinear terms in Equation [6] are needed to account for the beam-hardening effect. Equation [5] illustrates that the two sets of X-ray attenuation measurements are transformed into two sets of density projection measurements, and, as such, the reconstructed images represent the equivalent densities of the basis materials using the unit of $g \cdot cm^{-3}$ instead of the conventional linear attenuation coefficients, which use the unit of cm^{-1}.

It is noteworthy that material decomposition using dual-energy or spectral CT imaging does not identify the actual composition in each image voxel, but merely estimates the amount of each selected basis material required to produce the degrees of X-ray attenuation observed at the two applied energy spectra. Iodine-equivalent images (iodine maps) and water-equivalent images (virtual non-contrast images) acquired from dual-energy-based material decomposition are useful in several clinical applications.

Virtual Monochromatic Images

In addition to material-density images, virtual monochromatic images can also be generated from a set of dual-energy projections (40, 41). A virtual monochromatic image depicts how the imaged object would look like if a monochromatic beam of X-rays was used for imaging. For monochromatic imaging at a specific X-ray photon energy E_o, integration over the entire energy spectrum is not required, and Equation [5] can be simplified as:

$$P(E_o) = -ln\left(\frac{I}{I_o}\right) = D_I \cdot \left(\frac{\mu}{\rho}\right)_I(E_o) + D_W \cdot \left(\frac{\mu}{\rho}\right)_W(E_o) = \int \mu(\vec{r}, E_o)ds \quad [7]$$

Equation [7] indicates that a set of monochromatic projections can be derived from the equivalent density projections and mass attenuation coefficients of the basis materials, from which virtual monochromatic images can be reconstructed with the conventional filtered back projection algorithm. Alternatively, virtual monochromatic images can be generated from a simple linear operation of the material-density images that are generated from the material decomposition process discussed above (38, 40). In this approach, the value of any image voxel in a virtual monochromatic image is normalized to the attenuation value of water, as in standard CT images:

$$Im(x, y, E_o) = \frac{\sigma_I\rho(x,y)\cdot\mu_I(E_o) + \sigma_W\rho(x,y)\cdot\mu_W(E_o)}{\mu_W(E_o)}$$
$$= \sigma_W\rho(x, y) + \sigma_I\rho(x, y) \cdot \frac{\mu_I(E_o)}{\mu_W(E_0)} \quad [8]$$

where $Im(x, y, E_0)$ represents the value of an image voxel at coordinate (x, y) that corresponds to a monochromatic energy E_o. As discussed above, $\sigma_W\rho$ and $\sigma_I\rho$ are the equivalent densities of water and iodine, respectively. Given the known linear attenuation coefficient values of water and iodine over the entire range of diagnostic energies (20–150 keV), virtual monochromatic images can be readily generated with a unit of Hounsfield units (HUs) (Fig. 4). Virtual monochromatic imaging with dual-energy acquisition has useful clinical applications, including beam-hardening correction in myocardial perfusion measurements using CT. When a polychromatic beam of X-rays traverses through the imaged object, low-energy X-ray photons are preferentially attenuated first due to the photoelectric effect, and the effective energy of the X-ray beam increases (the beam is 'hardened') (42). In CT myocardial perfusion imaging, the presence of iodinated contrast solution in the heart chambers leads to inconsistent X-ray attenuation (and sequentially inconsistent X-ray effective energies) among different ray paths, which results in errors in image reconstruction. Because the root cause of the beam-hardening artifact is the polychromatic nature of X-rays, virtual monochromatic contrast-enhanced heart images are theoretically less affected by the beam-hardening artifact, permitting a more accurate assessment of myocardial perfusion based on the degree of contrast enhancement in the myocardium (43).

Multi-Material Decomposition

There are many clinical applications in which more than two materials are present in each image voxel, which poses challenges for the binary material decomposition technique discussed above. Methods that use the K-edge effect have been proposed for simultaneous decomposition of multiple

https://doi.org/10.3348/kjr.2020.0144

Korean Journal of Radiology
KJR

materials (44, 45) (Fig. 5), though these approaches require the use of photon-counting or multi-energy imaging, which is currently not available for clinical use. Alternatively, post-processing algorithms have been proposed for material decomposition in situations where more than two materials are present (46-48). Since only two sets of X-ray attenuation measurements are collected in a dual-energy scan, additional assumptions are needed to handle

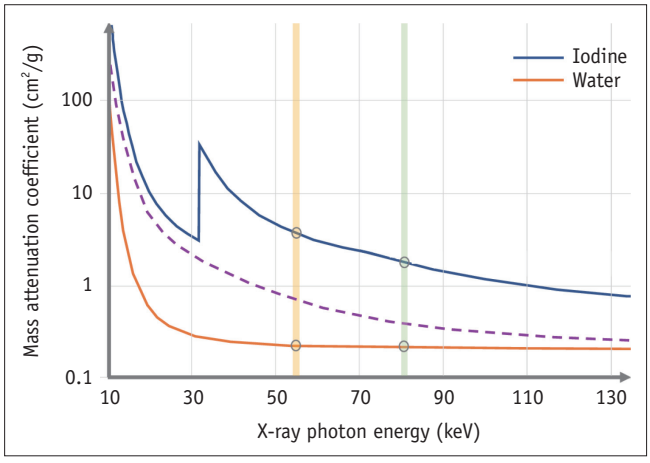

Fig. 4. Mass attenuation coefficients of iodine (solid blue curve) and water (solid orange curve) as a function of X-ray photon energy. The mass attenuation coefficient of an unknown material (calcium in this example, represented by a dotted purple curve) over the X-ray energy range in diagnostic CT can be approximately represented as a linear combination of two basis materials, iodine and water, except at the K-edge energy of iodine. The amount of iodine and water required to represent the material of interest can be estimated at two different X-ray photon energies (marked by the yellow and green bars).

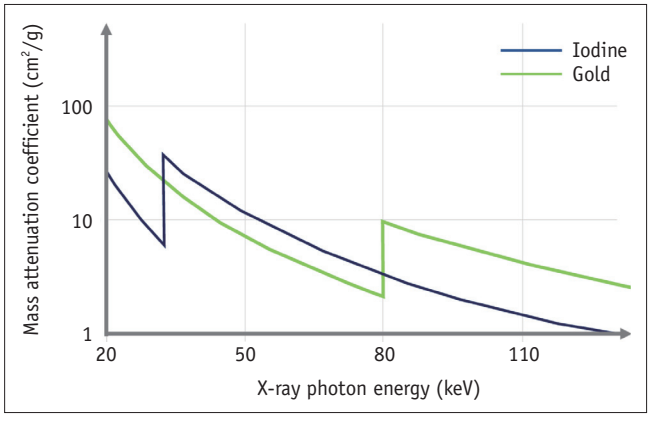

Fig. 5. Comparison of the mass attenuation coefficients of iodine and gold and their respective K-edge energies. The graph illustrates that multi-energy CT acquisition can be used to separate the attenuation signals between conventional iodine-based contrast agent and novel gold-based lipoprotein nanoparticle contrast agent. Preliminary results from preclinical studies suggest that the gold-based contrast agent may be useful for assessing the contents of an atherosclerotic plaque to determine if it is vulnerable to rupture (44).

three or more unknown quantities (material densities). One assumption commonly employed for this purpose is the conservation of mass and volume (47, 48). Suppose an image voxel contains N number of basis materials, with an N greater than 2. In this case, Equaton [3] can be rewritten as:

$$\mu(E) = \sum_{j=1}^{N} \sigma_j \rho \cdot \left(\frac{\mu}{\rho}\right)_j (E) \quad [9]$$

According to the assumption of the conservation of mass and volume, the total mass and volume of the mixed material in an image voxel equals the sum of the mass and volume of individual constituent (basis) materials. Hence, the equivalent density of the mixed material in Equation [9] can be represented by the sum of the masses of individual constituent materials divided by the total volume of the constituent materials:

$$\mu(E) = \sum_{j=1}^{N} \frac{m_j}{V} \cdot \left(\frac{\mu}{\rho}\right)_j (E)$$

where

$$V = \sum_{j=1}^{N} v_j \quad [10]$$

Equation [10] can be rewritten in the following form:

$$\mu(E) = \sum_{j=1}^{N} \frac{v_j}{V} \cdot \left(\frac{m_j}{v_j}\right)\left(\frac{\mu}{\rho}\right)_j (E)$$

$$= \sum_{j=1}^{N} \frac{v_j}{V} \cdot \mu_j(E)$$

For the special case of N = 3:

$$\mu(E) = \frac{v_1}{V}\mu_1(E) + \frac{v_2}{V}\mu_2(E) + \frac{v_3}{V}\mu_3(E)$$

$$= \frac{v_1}{V}\mu_1(E) + \frac{v_2}{V}\mu_2(E) + \frac{1-v_1-v_2}{V}\mu_3(E) \quad [11]$$

where $\frac{v_j}{V}$ is the volume fraction of the constituent (basis) material j, and the sum of the volume fraction of each basis material equals unity. The above equations illustrate how the assumption of the conservation of mass and volume can be useful for the estimation of three unknowns (material densities) given two attenuation measurements. If we select three basis materials that are sufficiently different from each other in terms of X-ray attenuation, the CT numbers that correspond to the low- and high-energy spectra can be plotted in a two-dimensional space to create a triangle (Fig. 6). Any unknown material for which the CT number pairs from the low- and high-energy images fall

https://doi.org/10.3348/kjr.2020.0144

within the triangle can be represented by the three basis materials, with the volume fraction of each basis material given by the area coordinates (49). The three-material decomposition algorithm is useful for contrast-enhanced CT studies in which iodine-based contrast medium is intravenously administered to the tissue region of interest. For example, the materials encountered in a liver perfusion study include fat, liver tissue, and iodine. Given that the X-ray attenuation of these materials as a function of X-ray energy is known, the proportion of each material required to contribute to the measured X-ray attenuation in each image voxel can be estimated.

Assessment of Tissue Stopping Power to Charged Particles

Cancer is one of the leading causes of mortality in the world, and radiotherapy is frequently used for killing cancerous cells. Radiotherapy with protons or heavy ions allows for a more localized dose deposition, which sequentially minimizes the damage to the normal tissues surrounding the targeted tumor. An accurate estimation of tissue stopping power is necessary for treatment planning during proton and heavy-ion radiotherapy (50). The average energy loss of charged particles per distance traversed in a material can be approximately estimated using the Bethe formula, which demonstrates that the stopping power of a material to charged particles is partially dependent on the electron density of the material (51). The electron density of a material can be readily assessed with dual-energy or spectral CT imaging (52-54). The underlying rationale is that the two basis functions (f_p and f_c) in Equation [1], which describe the photoelectric effect and Compton scattering, can also be replaced by basis functions that relate to other material properties, including electron density and atomic number. Previous studies have shown that the electron density of a material relative to that of water (relative electron density) is proportional to the stopping power of the material to swift ions (55), and the relative electron density holds an approximately linear relationship with the CT numbers (56). This linear relationship can be illustrated by the following equation (57):

$$\varrho_e = (1-d)\cdot\left(\frac{\mu_m(E_1)}{\mu_w(E_1)}\right) + d\cdot\left(\frac{\mu_m(E_2)}{\mu_w(E_2)}\right) \quad [12]$$

where ϱ_e is the relative electron density of the material m; μ_m is the linear attenuation coefficient of the material m; μ_w is the linear attenuation coefficient of water; and d

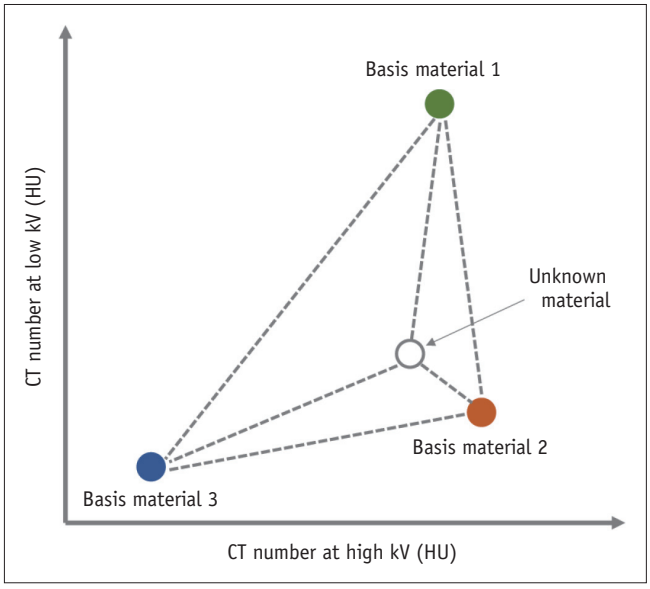

Fig. 6. Illustration of three-material decomposition with two-dimensional mapping of the CT numbers (in HU) measured from a dual-energy scan. In this example, any unknown material that falls within the triangle defined by the HU-pairs of the three selected basis materials can be represented as a linear combination of these basis materials. The volume fraction of each basis material can be determined from the corresponding vertices in the map.

is a constant that is dependent on the two selected X-ray energy spectra E_1 and E_2, which can be determined from calibration scans. Recall the definition of a HU:

$$HU = \left(\frac{\mu_m - \mu_w}{\mu_w}\right) \times 1000 \quad [13]$$

Equation [13] can be rewritten as:

$$\frac{HU}{1000} = \frac{\mu_m}{\mu_w} - \frac{\mu_w}{\mu_w}$$
$$\frac{\mu_m}{\mu_w} - 1 = \frac{HU}{1000}$$
$$\frac{\mu_m}{\mu_w} = \frac{HU}{1000} + 1 \quad [14]$$

Substituting Equation [14] into Equation [12] yields:

$$\varrho_e = (1-d)\cdot\left(\frac{HU_{E1}}{1000}+1\right) + d\cdot\left(\frac{HU_{E2}}{1000}+1\right) \quad [15]$$

Equation [15] offers a simple way to convert CT numbers measured in a dual-energy scan to the relative electron density of the material of interest on a voxel-by-voxel basis. It has been shown that the HU-ϱ_e conversion should be linear for materials with atomic numbers less than that of iodine (54) and that the errors of such conversions in soft tissues and bones are 2% or less (16). In addition

https://doi.org/10.3348/kjr.2020.0144

Korean Journal of Radiology
KJR

to calculating the relative electron density, dual-energy imaging has also been used to estimate the effective atomic number, which reflects the average atomic number in a mixture of materials and is also related to the stopping power to charged particles. It has been suggested that the additional information provided by the effective atomic number may facilitate the differentiation of different tissue types with very similar electron densities, though the actual usefulness in clinical applications remains to be fully explored.

Conflicts of Interest

The authors have no potential conflicts of interest to disclose.

REFERENCES

1. Flohr TG, McCollough CH, Bruder H, Petersilka M, Gruber K, Süss C, et al. First performance evaluation of a dual-source CT (DSCT) system. *Eur Radiol* 2006;16:256-268
2. Flohr TG, Bruder H, Stierstorfer K, Petersilka M, Schmidt B, McCollough CH. Image reconstruction and image quality evaluation for a dual source CT scanner. *Med Phys* 2008;35:5882-5897
3. Flohr TG. CT systems. *Curr Radiol Rep* 2013;1:52-63
4. Kyriakou Y, Kalender WA. Intensity distribution and impact of scatter for dual-source CT. *Phys Med Biol* 2007;52:6969-6989
5. Petersilka M, Stierstorfer K, Bruder H, Flohr T. Strategies for scatter correction in dual source CT. *Med Phys* 2010;37:5971-5992
6. Li B, Yadava G, Hsieh J. Quantification of head and body $CTDI_{VOL}$ of dual-energy x-ray CT with fast-kVp switching. *Med Phys* 2011;38:2595-2601
7. Zhang D, Li X, Liu B. Objective characterization of GE Discovery CT750 HD scanner: gemstone spectral imaging mode. *Med Phys* 2011;38:1178-1188
8. So A, Lee TY, Imai Y, Narayanan S, Hsieh J, Kramer J, et al. Quantitative myocardial perfusion imaging using rapid kVp switch dual-energy CT: preliminary experience. *J Cardiovasc Comput Tomogr* 2011;5:430-442
9. Hsieh J, Gurmen OE, King KF. Investigation of a solid-state detector for advanced computed tomography. *IEEE Trans Med Imaging* 2000;19:930-940
10. Nikl M. Scintillation detectors for x-rays. *Meas Sci Technol* 2006;17:R37-R54
11. Shkumat NA, Siewerdsen JH, Dhanantwari AC, Williams DB, Richard S, Paul NS, et al. Optimization of image acquisition techniques for dual-energy imaging of the chest. *Med Phys* 2007;34:3904-3915
12. Chaytor RJ, Rajbabu K, Jones PA, McKnight L. Determining the composition of urinary tract calculi using stone-targeted dual-energy CT: evaluation of a low-dose scanning protocol in a clinical environment. *Br J Radiol* 2016;89:20160408
13. Chandramohan M. *Dual energy composition analysis. Case study*. Canon Medical Systems Corporation, 2018. Available at: https://mfl.ssl.cdn.sdlmedia.com/636673921901874788AG.pdf. Accessed January, 2020
14. Bornefalk H, Danielsson M. Photon-counting spectral computed tomography using silicon strip detectors: a feasibility study. *Phys Med Biol* 2010;55:1999-2022
15. Roessl E, Herrmann C, Kraft E, Proksa R. A comparative study of a dual-energy-like imaging technique based on counting-integrating readout. *Med Phys* 2011;38:6416-6428
16. Hua CH, Shapira N, Merchant TE, Klahr P, Yagil Y. Accuracy of electron density, effective atomic number, and iodine concentration determination with a dual-layer dual-energy computed tomography system. *Med Phys* 2018;45:2486-2497
17. McCollough CH, Leng S, Yu L, Fletcher JG. Dual- and multi-energy CT: principles, technical approaches, and clinical applications. *Radiology* 2015;276:637-653
18. Euler A, Parakh A, Falkowski AL, Manneck S, Dashti D, Krauss B, et al. Initial results of a single-source dual-energy computed tomography technique using a split-filter: assessment of image quality, radiation dose, and accuracy of dual-energy applications in an in vitro and in vivo study. *Invest Radiol* 2016;51:491-498
19. Almeida IP, Schyns LE, Öllers MC, van Elmpt W, Parodi K, Landry G, et al. Dual-energy CT quantitative imaging: a comparison study between twin-beam and dual-source CT scanners. *Med Phys* 2017;44:171-179
20. Shikhaliev PM. Energy-resolved computed tomography: first experimental results. *Phys Med Biol* 2008;53:5595-5613
21. Herrmann C, Engel KJ, Wiegert J. Performance simulation of an x-ray detector for spectral CT with combined Si and Cd[Zn]Te detection layers. *Phys Med Biol* 2010; 55:7697-7713
22. Persson M, Huber B, Karlsson S, Liu X, Chen H, Xu C, et al. Energy-resolved CT imaging with a photon-counting silicon-strip detector. *Phys Med Biol* 2014;59:6709-6727
23. Muenzel D, Bar-Ness D, Roessl E, Blevis I, Bartels M, Fingerle AA, et al. Spectral photon-counting CT: initial experience with dual-contrast agent K-edge colonography. *Radiology* 2017;283:723-728
24. Yu Z, Leng S, Jorgensen SM, Li Z, Gutjahr R, Chen B, et al. Evaluation of conventional imaging performance in a research whole-body CT system with a photon-counting detector array. *Phys Med Biol* 2016;61:1572-1595
25. Mijnheer BJ, Guldbakke S, Lewis VE, Broerse JJ. Comparison of the fast-neutron sensitivity of a Geiger-Müller counter using different techniques. *Phys Med Biol* 1982;27:91-96
26. Garcia-Sanchez AJ, Garcia Angosto EA, Moreno Riquelme PA, Serna Berna A, Ramos-Amores D. Ionizing radiation measurement solution in a hospital environment. *Sensors (Basel)* 2018;18:510
27. Yamada H, Suzuki A, Uchida Y, Yoshida M, Yamamoto H, Tsukuda Y. A scintillator Gd_2O_2S: Pr, Ce, F for X-ray computed tomography. *J Electrochem Soc* 1989;136:2713-2716
28. Rossner W, Ostertag M, Jermann F. Properties and applications

 https://doi.org/10.3348/kjr.2020.0144

of gadolinium oxysulfide based ceramic scintillators. *Electrochem Soc Proc* 1999;98:187-194
29. Li B. Dual-energy CT with fast-kVp switching and its applications in orthopedics. *OMICS J Radiol* 2013;2:137
30. Taguchi K, Iwanczyk JS. Vision 20/20: single photon counting x-ray detectors in medical imaging. *Med Phys* 2013;40:100901
31. Taguchi K, Zhang M, Frey EC, Wang X, Iwanczyk JS, Nygard E, et al. Modeling the performance of a photon counting x-ray detector for CT: energy response and pulse pileup effects. *Med Phys* 2011;38:1089-1102
32. Persson M, Bujila R, Nowik P, Andersson H, Kull L, Andersson J, et al. Upper limits of the photon fluence rate on CT detectors: case study on a commercial scanner. *Med Phys* 2016;43:4398-4411
33. Shikhaliev PM, Fritz SG, Chapman JW. Photon counting multienergy x-ray imaging: effect of the characteristic x rays on detector performance. *Med Phys* 2009;36:5107-5119
34. Xu C, Danielsson M, Bornefalk H. Evaluation of energy loss and charge sharing in cadmium telluride detectors for photon-counting computed tomography. *IEEE Trans Nucl Sci* 2011;58:614-625
35. Szeles C, Soldner SA, Vydrin S, Graves J, Bale DS. CdZnTe semiconductor detectors for spectroscopic x-ray imaging. *IEEE Trans Nucl Sci* 2008;55:572-582
36. Alvarez RE, Macovski A. Energy-selective reconstructions in X-ray computerized tomography. *Phys Med Biol* 1976;21:733-744
37. Lehmann LA, Alvarez RE, Macovski A, Brody WR, Pelc NJ, Riederer SJ, et al. Generalized image combinations in dual KVP digital radiography. *Med Phys* 1981;8:659-667
38. Hubbell JH, Seltzer SM. *Tables of x-ray mass attenuation coefficients and mass energy-absorption coefficients 1 keV to 20 MeV for elements Z=1 to 92 and 48 additional substances of dosimetric interest*. Gaithersburg: National Institute of Standards and Technology, 1996
39. Hsieh J. *Advanced CT applications*. In: Hsieh J, ed. *Computed tomography principles, design, artifacts and recent advances*, 2nd ed. Hoboken: Wiley, 2009:469-543
40. Wu X, Langan DA, Xu D, Benson TM, Pack JD, Schmitz AM, et al. *Monochromatic CT image representation via fast switching dual kVp*. SPIE Medical Imaging;2009 March 13;Lake Buena Vista, USA
41. Yu L, Leng S, McCollough CH. Dual-energy CT-based monochromatic imaging. *AJR Am J Roentgenol* 2012;199:S9-S15
42. Brooks RA, Di Chiro G. Beam hardening in x-ray reconstructive tomography. *Phys Med Biol* 1976;21:390-398
43. So A, Hsieh J, Imai Y, Narayanan S, Kramer J, Procknow K, et al. Prospectively ECG-triggered rapid kV-switching dual-energy CT for quantitative imaging of myocardial perfusion. *JACC Cardiovasc Imaging* 2012;5:829-836
44. Cormode DP, Roessl E, Thran A, Skajaa T, Gordon RE, Schlomka JP, et al. Atherosclerotic plaque composition: analysis with multicolor CT and targeted gold nanoparticles. *Radiology* 2010;256:774-782
45. Schlomka JP, Roessl E, Dorscheid R, Dill S, Martens G, Istel T, et al. Experimental feasibility of multi-energy photon-counting K-edge imaging in pre-clinical computed tomography. *Phys Med Biol* 2008;53:4031-4047
46. Johnson TR, Krauss B, Sedlmair M, Grasruck M, Bruder H, Morhard D, et al. Material differentiation by dual energy CT: initial experience. *Eur Radiol* 2007;17:1510-1517
47. Liu X, Yu L, Primak AN, McCollough CH. Quantitative imaging of element composition and mass fraction using dual-energy CT: three-material decomposition. *Med Phys* 2009;36:1602-1609
48. Mendonca PR, Lamb P, Sahani DV. A flexible method for multi-material decomposition of dual-energy CT images. *IEEE Trans Med Imaging* 2014;33:99-116
49. Hsieh J. *Advanced CT applications*. In: Hsieh J, ed. *Computed tomography principles, design, artifacts and recent advances*, 3rd ed. Bellingham: SPIE Press Book, 2015:529-623
50. van Elmpt W, Landry G, Das M, Verhaegen F. Dual energy CT in radiotherapy: current applications and future outlook. *Radiother Oncol* 2016;119:137-144
51. Grimes DR, Warren DR, Partridge M. An approximate analytical solution of the Bethe equation for charged particles in the radiotherapeutic energy range. *Sci Rep* 2017;7:9781
52. Torikoshi M, Tsunoo T, Sasaki M, Endo M, Noda Y, Ohno Y, et al. Electron density measurement with dual-energy x-ray CT using synchrotron radiation. *Phys Med Biol* 2003;48:673-685
53. Goodsitt MM, Christodoulou EG, Larson SC. Accuracies of the synthesized monochromatic CT numbers and effective atomic numbers obtained with a rapid kVp switching dual energy CT scanner. *Med Phys* 2011;38:2222-2232
54. Saito M. Potential of dual-energy subtraction for converting CT numbers to electron density based on a single linear relationship. *Med Phys* 2012;39:2021-2030
55. Matsufuji N, Tomura H, Futami Y, Yamashita H, Higashi A, Minohara S, et al. Relationship between CT number and electron density, scatter angle and nuclear reaction for hadron-therapy treatment planning. *Phys Med Biol* 1998;43:3261-3275
56. Mustafa AA, Jackson DF. The relation between X-ray CT numbers and charged particle stopping powers and its significance for radiotherapy treatment planning. *Phys Med Biol* 1983;28:169-176
57. Hünemohr N, Krauss B, Tremmel C, Ackermann B, Jäkel O, Greilich S. Experimental verification of ion stopping power prediction from dual energy CT data in tissue surrogates. *Phys Med Biol* 2014;59:83-96

https://doi.org/10.3348/kjr.2020.0144